POLITECNICO DI TORINO
Repository ISTITUZIONALE

Coherent Modelling Switch Between Pointwise and Distributed Representations of Cell Aggregates

(Article begins on next page)

26 April 2024

Coherent modelling switch between pointwise and distributed representations of cell aggregates

A. Colombi · M. Scianna · L. Preziosi

Abstract Biological systems are typically formed by different cell phenotypes, characterized by specific biophysical properties and behaviors. Moreover, cells are able to undergo differentiation or phenotypic transitions upon internal or external stimuli. In order to take these phenomena into account, we here propose a modelling framework in which cells can be described either as pointwise/concentrated particles or as distributed masses, according to their biological determinants. A set of suitable rules then defines a coherent procedure to switch between the two mathematical representations. The theoretical environment describing cell transition is then enriched by including cell migratory dynamics and duplication/apoptotic processes, as well as the kinetics of selected diffusing chemicals influencing the system evolution. Finally, biologically relevant numerical realizations are presented: in particular, they deal with the growth of a tumor spheroid and with the initial differentiation stages of the formation of the zebrafish posterior lateral line. Both phenomena mainly rely on cell phenotypic transition and differentiated behaviour, thereby constituting biological systems particularly suitable to assess the advantages of the proposed model.

Keywords multiscale modeling · hybrid systems · cell differentiation · cell phenotypic transition · multiscale dynamics

1 Introduction

Biological systems are characterized by collective dynamics that arise from individual behaviors and interactions through multiscale interconnected processes. More specifically, the evolution of macroscopic cell aggregates, visible

A. Colombi · M. Scianna (E-mail: marcosci1@alice.it) · L. Preziosi
Department of Mathematical Sciences "G. L. Lagrange", Politecnico di Torino
Corso Duca degli Abruzzi 24, 10129 Torino, Italy

by looking at the totality of cells as a whole, results from the phenomenology of the single component cells.

Entering in more details, collective cell movement is the principal migration modes in morphogenesis, regeneration and cancer, and depend upon complex cell-cell (and cell-tissue) interactions [16], [21]. In particular, most biological systems are composed by multiple cell populations, or multiple clones of the same population, with specific functions and migratory determinants. For instance, few specialized cells typically behave as a patterning guidance for the rest of the aggregate [21], [23]. These phenomena are mainly regulated by both temporary activations and long-lasting differentiation processes, that are able to define the leader individuals within the moving cell group [16].

A relevant example of such regulatory mechanisms is the so-called tip cell selection and lateral inhibition, which establishes the leader endothelial cells during physio-pathological vascularization. This process is mediated by selected vascular endothelial growth factor (VEGF)-induced delta-notch signaling pathways [24], [28], [29], [37] and references therein. Another example is given by the epithelial-to-mesenchymal transition (EMT), which is instead typical of different stages of morphogenesis and organogenesis in addition to the development of carcinomas (i.e., tumors of epithelial origin, such as lung, breast, ovarian, and prostate malignancies). This process, caused by a dramatic loss of cell-cell adhesive junctions, consists in the delamination (and in the subsequent individual invasion of the mesenchyme also via proteolytic activity) of groups of aggressive cells from epithelial layers [16]. In this respect, EMT-like dynamics also comprehend those processes where the downregulation of intercellular adhesive interactions results in cell detachment and in the onset of single-cell modes of migration.

From a mathematical point of view, it is indeed desirable to develop modelling structures able to capture and represent different cell behaviours as well as the relative mechanisms of phenotypic transitions. In this respect, we here present an innovative modelling approach, which allows a cell aggregate to be described either as a set of pointwise/concentrated particles or through its spatial mass density. Further, our mathematical environment allows to pass from a localized to a distributed representation of the single component cells by defining a proper *bubble function*, which represents the spatial mass extension of each individuals. In this respect, the basic idea is that cell transition can be modeled through the substitution of a localized mass with the relative bubble function, and *viceversa* (see the left panels in Fig. 1).

In order to apply the proposed approach to specific biological problems, the resulting hybrid model is finally enriched with proper equations describing the behavior of each cell clone, i.e., cell migratory dynamics, duplication/apoptosis processes, as well as the kinetics of extracellular chemicals or other involved phenomena (see again Fig. 1). In particular, in this context, selected chemical stimuli may assume a relevant role both in influencing system dynamics and growth/death processes and in triggering cell phenotypic differentiations, with the consequent switch of cell mathematical representation.
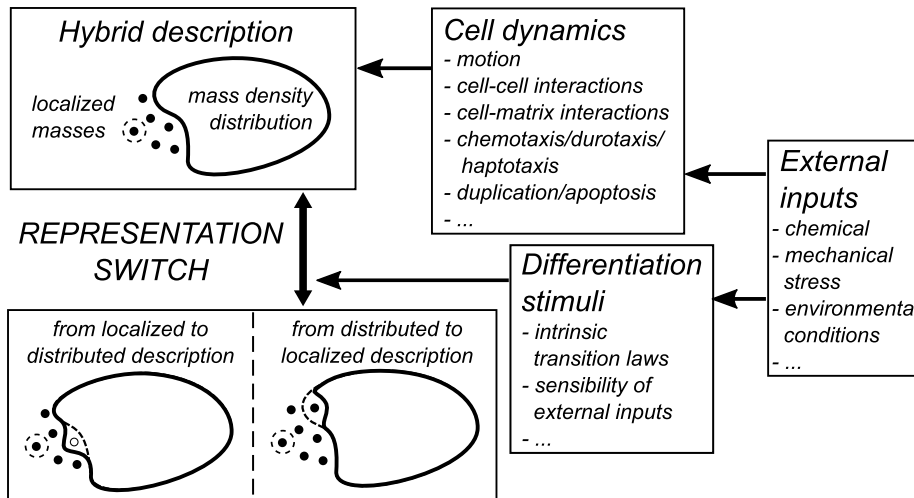
Fig. 1 Conceptual scheme of model: Our mathematical environment allows to account both for cell phenotypic transitions and for cell migratory dynamics and patterning. Key features of our approach are the use of different descriptive instances (i.e., localized vs. distributed) for cells characterized by different behaviors and properties (i.e., activated vs. deactivated) and the definition of a coherent procedure to describe cell phenotypic differentiations.

The remaining part of the article is organized as follows. In Section 2, we present the main model features, supported by a sample test application that shows how the multiscale cell differentiation procedure works. Section 3 is then devoted to the application of the model to some relevant biological problems, i.e., avascular tumor expansion and invasion and zebrafish posterior lateral line (pLL) development.

2 Modelling the localized/distributed switch

An aggregate of N cells can be mathematically described either as a set of localized individual particles or through the spatial distribution of its mass density, according to the phenomenon of interest. Such different cell representations may also coexist in the case of biological systems formed by different cell lines or by distinct clones of the same cell lineage, whose specific properties and behaviour justify the convenience of adopting different descriptive instances. In this respect, we here propose a mathematical framework that allows both types of cell representations as well as rules for dynamic transition between them. In the following, we will refer to a generic two dimensional domain $\Omega \subseteq \mathbb{R}^2$: however, the methodology can be easily extended also to three-dimensional environments.

Purely localized/pointwise description. From this point of view, each cell of the aggregate is represented as a dimensionless point with concentrated mass $\overline{m}$, and identified by its position in space, i.e., $\mathbf{x}_j(t) \in \Omega$ with $j = 1, \ldots, N(t)$,

where $N(t)$ is the total number of cells, possibly varying in time following suitable growth/death laws assuring that $N(t) \in \mathbb{N}$ for any t In this respect, the configuration of the entire aggregate at a given time t is defined by the following vector:

$$\mathbf{X}(t) = \{\mathbf{x}_1(t),\ \mathbf{x}_2(t),\ \ldots,\ \mathbf{x}_{N(t)}(t)\}, \tag{1}$$

with $N(t) \in \mathbb{N}$, and the mass of the whole aggregate is given by $M(t) = \overline{m}N(t)$.

Purely distributed description. On the other hand, the configuration of the system can be completely described by defining a spatial mass density distribution $\rho(t, \mathbf{y}) : \mathbb{R}_+ \times \Omega \to \mathbb{R}_+$ such that

$$\int_\Omega \rho(t, \mathbf{y})d\mathbf{y} = M(t)\ \ \forall\, t. \tag{2}$$

In this respect, ρ has units $\mu\mathrm{g}/\mu\mathrm{m}^2$, and the mass of the whole aggregate $M(t) \in \mathbb{R}_+$, for any t, represents $N(t) = \lfloor M(t)/\overline{m} \rceil$ cells. In this context, $M(t)$ possibly varies in time according to suitable growth/death laws for the mass density ρ (such as, for instance, exponential or logistic laws).

Hybrid description. As already seen, a cellular system can be composed of subpopulations which have equal biophysical properties (e.g., shape, dimension) but different behaviours. In these situations, it can be convenient to use a distinct mathematical representation for each cell subgroup

$$\mathbf{X}(t) = \{\mathbf{x}_1(t),\ \mathbf{x}_2(t),\ \ldots,\ \mathbf{x}_{N_L(t)}\};$$

$$\rho(t, \mathbf{y})\ :\ \int_\Omega \rho(t, \mathbf{y})d\mathbf{y} = M_D(t)\ \ \forall\, t, \tag{3}$$

i.e., to differentiate the aggregate in two subsystems: one composed of $N_L(t) \in \mathbb{N}$ localized cells and the other formed by the distributed mass $M_D(t) \in \mathbb{R}_+$, such that $\overline{m}\, N_L(t) + M_D(t)$ gives the mass $M(t)$ of the whole aggregate, for any t. In particular, from a biological point of view, a localized/pointwise description is more appropriate for *activated/differentiated* cells, whereas a distributed representation, characterized by a lower level of individual details, is more suitable for *quiescent/undifferentated* cell ensembles. Keeping in mind the above-considerations, in this case, possible growth/death processes of each clone are reproduced by defining proper laws for $N_L(t) \in \mathbb{N}$ and $\rho(t)$, respectively. In particular, the duplication/apoptosis of localized cells results in stepwise mass variations, whereas growth/death processes of the distributed part of the aggregate result in continuous variations.

In a wide range of biological processes, individual cells undergo phenotypic transitions, i.e., they can activate or deactivate. These mechanisms can be reproduced in our framework by assuming a hybrid description of the system and allowing a switch between the two cell descriptive instances: it is indeed necessary to define a proper correspondence between the localized and the
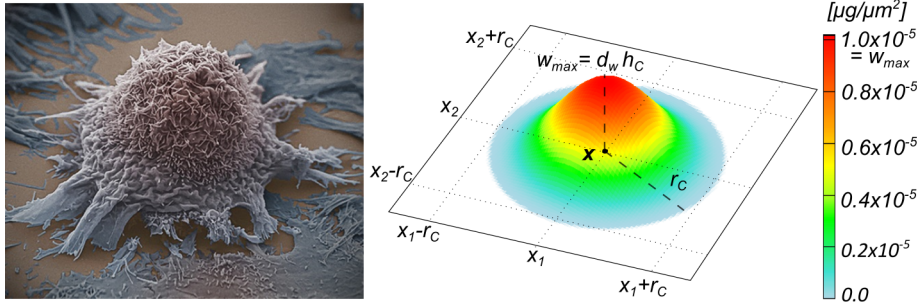
Fig. 2 Left panel: Representative morphology of a cell seeded on a planar substrate, image taken from `http://www.cell.com/pictureshow/cell-motility`. Right panel: Selected form of bubble function $w_\mathbf{x}$ describing the mass extension of a cell centered in $\mathbf{x} = (x_1, x_2)$, see Eq. (5).

distributed representation of a single cell. In this respect, let us first introduce a function $w_\mathbf{x}(\mathbf{y}) : \Omega \times \Omega \to \mathbb{R}_+$, that will be denoted as *bubble function*, such that

$$\int_\Omega w_\mathbf{x}(\mathbf{y}) d\mathbf{y} = \overline{m}. \qquad (4)$$

It has units $\mu g/\mu m^2$ and models the spatial mass distribution of a cell whose center is located in $\mathbf{x} \in \Omega$. In principle, there exist several possible options to properly explicit the form of $w_\mathbf{x}$. However, as reproduced in Fig. 2, the typical morphology of cells seeded on planar substrates can be well approximated by the following bubble function:

$$w_\mathbf{x}(\mathbf{y}) = \begin{cases} \dfrac{d_w\, h_c}{r_c^6} \left(r_c^2 - |\mathbf{x} - \mathbf{y}|^2 \right)^3, & \text{if } |\mathbf{x} - \mathbf{y}| < r_c; \\[2mm] 0, & \text{otherwise}; \end{cases} \qquad (5)$$

where $|\cdot|$ identifies the modulus of a vector in the Euclidean norm. In the case of our interest, $d_w \approx 10^3$ kg/m^3 is the density of water (which is the main constituent of cells [1]), $r_c = 15\ \mu m$ is the mean cell radius and $h_c = 10\ \mu m$ is the cell "height", established by considering that cells have to contain the voluminous stiff nucleus (whose dimensions fall in the range $7 - 10\ \mu m$ [1]). These values allow to estimate the cell mass $\overline{m} = (\pi/4)d_w h_c r_c^2 = 1.8 \cdot 10^{-9}$ g $= 1.8 \cdot 10^{-3}\ \mu g$, which is consistent with the measurements performed in [6].

Referring to the hybrid representation of an aggregate of mass $M(t)$ given in Eq. (3), let us now assume that, at a certain time t, the j-th cell individually described and located in $\mathbf{x}_j(t)$ undergoes a phenotypic transition (i.e., a deactivation), thereby requiring a switch of its mathematical representation. Such a process can be implemented in our modelling framework by removing the localized cell j, centered at $\mathbf{x}_j$, from the pointwise representation $\mathbf{X}$ and by simultaneously adding the equivalent mass distribution function $w_{\mathbf{x}_j(t)}$ to

the density ρ. Consistently, both the number of localized cells and the overall mass of distributed cell have to be updated. In mathematical terms, we indeed get the following relations:

$$
\begin{cases}
N_L(t^+) = N_L(t) - 1; \\
M_D(t^+) = M_D(t) + \overline{m}; \\
\mathbf{X}(t^+) = \mathbf{X}(t) \setminus \{\mathbf{x}_j(t)\} = \{\mathbf{x}_i(t^+)\}_{i=1}^{N_L(t^+)}; \\
\rho(t^+, \mathbf{y}) = \rho(t, \mathbf{y}) + w_{\mathbf{x}_j(t)}(\mathbf{y}) \quad \forall\, \mathbf{y} \in \Omega,
\end{cases}
\tag{6}
$$

where the localized representation of the remaining $N_L(t^+)$ cells is renumbered according to the following rule

$$
\mathbf{x}_i(t^+) = \begin{cases}
\mathbf{x}_i(t), & \text{if } i < j; \\
\mathbf{x}_{i-1}(t), & \text{if } i > j.
\end{cases}
\tag{7}
$$

Remark. With respect to the characteristic time scales of other biological processes (movement, duplication, death), cell phenotypic transitions can be considered an almost instantaneous phenomenon. In this respect, we assume that, at each time t, cell differentiation results in an intermediate system configuration, identified by the time notation t^+.

In general, the above-described representation switch of cell j can be induced both by a prescribed intracellular input (e.g., intrinsic law) or by an evolving extracellular stimulus. In particular, from a biological point of view, cell phenotypic transitions are mainly triggered by molecular stimuli: for instance, high levels of selected chemicals activate cells, whereas low enough concentration of growth factors results in cell quiescence/deactivation. In this respect, let us assume that the local concentration of a molecular substance drops below a certain threshold in $\mathbf{x}_s \in \Omega$ at t: the above-described phenotypic differentiation actually occurs only if there is a localized cell j placed in $\mathbf{x}_s$, i.e., if there exists a j such that $\mathbf{x}_j(t) = \mathbf{x}_s$.

Let us then conversely assume that the same molecular variable exceeds the given threshold in $\mathbf{x}_s$, thereby stimulating cell activation mechanisms which require the inverse transition between the two mathematical descriptive instances. In this case, the representation switch is possible only if there is a sufficient amount of mass to have a localized cell centered in $\mathbf{x}_s$. This amounts to have a sufficient mass density distribution over all the support of $w_{\mathbf{x}_s}$, which, as seen, describes the distributed mass of a possible localized cell placed in $\mathbf{x}_s$ (i.e., to have $\rho(t, \mathbf{y}) \geq w_{\mathbf{x}_s}(\mathbf{y}), \; \forall \mathbf{y}$). If this condition is satisfied the cell phenotypic transition (and the corresponding representation switch) results from the removal of the mass distribution $w_{\mathbf{x}_s}$ from the density ρ, the addition of a

new localized cell $N_L + 1$ placed in $\mathbf{x}_s$ to the pointwise representation $\mathbf{X}$, and the update of both N_L and M_D:

$$
\begin{cases}
N_L(t^+) = N_L(t) + 1; \\[1ex]
M_D(t^+) = M_D(t) - \overline{m}; \\[1ex]
\mathbf{X}(t^+) = \mathbf{X}(t) \cup \{\mathbf{x}_s\} = \{\mathbf{x}_i(t^+)\}_{i=1}^{N_L(t^+)}; \\[1ex]
\rho(t^+, \mathbf{y}) = \rho(t, \mathbf{y}) - w_{\mathbf{x}_s}(\mathbf{y}) \quad \forall\, \mathbf{y} \in \Omega.
\end{cases}
\tag{8}
$$

In this case, the localized representation is renumbered as follows

$$
\mathbf{x}_i(t^+) =
\begin{cases}
\mathbf{x}_i(t), & \text{if } i < N_L(t^+); \\[1ex]
\mathbf{x}_s, & \text{if } i = N_L(t^+).
\end{cases}
\tag{9}
$$

The extension of the above-described procedure to the case of simultaneous phenotypic differentiations can be done as follows. We assume that, at a given time t, a set of $P(t)$ localized cells and a given amount of distributed mass, corresponding to $Q(t)$ cells, change phenotype under selected extracellular stimuli placed at $\{\mathbf{p}_1, \ldots, \mathbf{p}_P\}$ and $\{\mathbf{q}_1, \ldots, \mathbf{q}_Q\}$, respectively (with $\mathbf{p}_h, \mathbf{q}_k \in \Omega$ for any $h = 1, \ldots, P(t)$ and $k = 1, \ldots, Q(t)$). In order to actually have these transitions, we need that

(i) for each h, there exist a cell j such that $\mathbf{x}_j(t) = \mathbf{p}_h$;

(ii) $\rho(t, \mathbf{y}) \geq \sum\limits_{k=1}^{Q(t)} w_{\mathbf{q}_k}(\mathbf{y})$ for all $\mathbf{y} \in \Omega$.

If all these conditions are satisfied, we have

$$
\begin{cases}
N_L(t^+) = N_L(t) - P(t) + Q(t), \\[1ex]
M_D(t^+) = M_D(t) + \overline{m}(P(t) - Q(t)), \\[1ex]
\mathbf{X}(t^+) = \mathbf{X}(t) \setminus \{\mathbf{p}_1, \ldots, \mathbf{p}_{P(t)}\} \cup \{\mathbf{q}_1, \ldots, \mathbf{q}_{Q(t)}\} = \{\mathbf{x}_i(t^+)\}_{i=1}^{N_L(t^+)}, \\[1ex]
\rho(t^+, \mathbf{y}) = \rho(t, \mathbf{y}) + \sum\limits_{h=1}^{P(t)} w_{\mathbf{p}_h}(\mathbf{y}) - \sum\limits_{k=1}^{Q(t)} w_{\mathbf{q}_k}(\mathbf{y}) \quad \forall\, \mathbf{y} \in \Omega,
\end{cases}
\tag{10}
$$

where the localized representation is renumbered according to the rules given in Eq. (7) and (9). Finally, the generalization to more cell populations is straightforward.

Remark. If the condition for a distributed-to-localized cell transition is simultaneously satisfied in two or more points of the domain, resulting in an overlap of the corresponding bell functions, only a single cell differentiation occurs, whose location is randomly established.
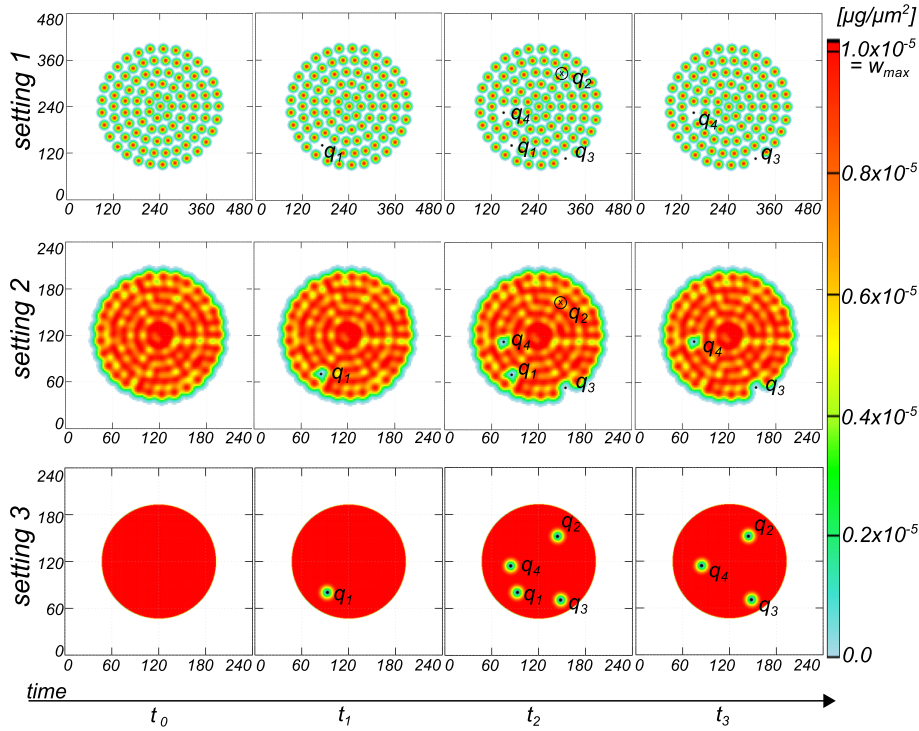
Fig. 3 Cell phenotypic differentiations (with the coherent switches between the corresponding mathematical descriptions) induced at successive instants by localized extracellular signals within initially quiescent cell systems. Setting 1: Cell aggregate composed by 95 detached bell functions $w_{(\cdot)}$. Setting 2: Cell aggregate formed by 95 overlapping bell functions $w_{(\cdot)}$. Setting 3: Cell colony characterized by a homogeneous mass density $w_{\max} = \max_{\mathbf{y} \in \mathbb{R}^2} \{w_{(\cdot)}(\mathbf{y})\}$. At t_1, a cell phenotypic transition is triggered in a single point $\mathbf{q}_1$, differently located within each aggregate. As a result, in all settings, a localized individual forms, surrounded by a round area with decreased mass density (which corresponds to the support of the bell function $w_{\mathbf{q}_1}$). Successively, at t_2, cell activation is stimulated in three different points for each aggregate. In the case of the initial configuration 3, cell phenotypic transitions are observed in all the three locations. For settings 1 and 2, cell activation actually occurs only in $\mathbf{q}_3$ and in $\mathbf{q}_4$: in both cases, the mass density distributed over the support of $w_{\mathbf{q}_2}$ is in fact not sufficient to constitute a differentiated individual. Finally, at t_3, the firstly activated cell located in $\mathbf{q}_1$ is assumed to turn back to the quiescent state as its period of differentiation has terminated: therefore, in all system configurations, the initial mass distribution is locally recovered.

2.1 Test simulation: dynamical change of cell representation

Before including in the picture intercellular interactions, it is useful to give an example of cell phenotypic transitions in the case of a colony whose cells do not move but undergo only differentiation at selected instant times. In particular, in all simulations, we start with a spheroid of initially quiescent cells, which are represented by a distributed density whose amount is equal to $95\,\overline{m}$ (i.e., to the mass of 95 cells). The exact initial mass configuration is arranged to

obtain 3 different settings (the domain Ω is resized accordingly, see the left panels in Fig. 3):

Setting 1: it consists of a set of 95 *disjoint* bubble functions, i.e.,

$$\rho(0, \mathbf{y}) = \sum_{j=1}^{95} w_{\mathbf{x}_j(0)}(\mathbf{y}) \ \ \forall \, \mathbf{y} \in \Omega, \tag{11}$$

where $w_{\mathbf{x}}$ is defined in Eq. (5) and, for any pair $(h, \ k)$ of first-nearest neighboring cells, $|\mathbf{x}_h - \mathbf{x}_k| = 30 \ \mu\text{m} > r_c$;

Setting 2: it consists of a set of 95 *overlapping* bubble functions, i.e., Eq. (11) holds but with the condition $|\mathbf{x}_h - \mathbf{x}_k| = 15 \ \mu\text{m} = r_c$ for any pair $(h, \ k)$ of first-nearest neighbors;

Setting 3: it consists of a round compact colony with homogeneous density equal to $w_{\max} = \max_{\mathbf{y} \in \mathbb{R}^2}\{w_{\mathbf{x}}(\mathbf{y})\} = d_w \ h_c = 10^{-5} \ \mu\text{g}/\mu\text{m}^2$, which is the maximal value taken by the bubble function $w_{\mathbf{x}}(\mathbf{y})$ (see Eq. (5)), and whose overall mass is equal to $95\overline{m}$, as in previous cases. In this case, we indeed have

$$\rho(0, \mathbf{y}) = \begin{cases} w_{\max}, \ \forall \, \mathbf{y} \in B_{r_{ag}}(120, 120); \\ \\ 0, \qquad \text{otherwise,} \end{cases} \tag{12}$$

where $B_{r_{ag}}(120, 120)$ is the ball centered in $(120 \ \mu\text{m}, 120 \ \mu\text{m})$ with radius $r_{ag} = \sqrt{95\overline{m}/(\pi w_{\max})} = 73.8 \ \mu\text{m}$. It is worth noting that, in case of homogeneous distribution of cells, $w_{\max}$ is the minimum value of mass density that allows the switch from a distributed to localized representation of cells.

Referring to the hybrid system representation given in Eq. (3), in all the above-described settings we have that $N_L(0) = 0$, $M_D(0) = 95\overline{m}$, $\mathbf{X}(0) = \emptyset$.

At a given time t_1, an external input stimulates cell phenotypic transition in a single point ($\mathbf{q}_1 = (171.6 \ \mu\text{m}, 141.4 \ \mu\text{m})$ in the case of setting 1, $\mathbf{q}_1 = (85.8 \ \mu\text{m}, 70.7 \ \mu\text{m})$ in the case of setting 2, and $\mathbf{q}_1 = (92.4 \ \mu\text{m}, 80.3 \ \mu\text{m})$ in the case of setting 3). As reproduced in Fig. 3, for all system configurations, a sufficient amount of distributed mass is located over the support of $w_{\mathbf{q}_1}$ (i.e., $\rho(t_1, \mathbf{y}) \geq w_{\mathbf{q}_1}(\mathbf{y})$, $\forall \mathbf{y} \in \Omega$), so that cell activation actually occurs leading to the corresponding switch between the mathematical cell descriptions. In particular, in the first two settings, $\mathbf{q}_1$ is exactly located in the center of one of the bubble functions used to establish the initial condition of the aggregate, whereas in the third setting $\mathbf{q}_1$ falls within the colony, which, as already said, is characterized by a high enough constant density to allow cell differentiation (see Eq. (12)). As a result, in all settings (but with a clear evidence in the case of setting 3), the localized cell formed in $\mathbf{q}_1$ is surrounded by a round area of radius r_c characterized by a reduction of the local mass density: it corresponds to the support of the bell function $w_{\mathbf{q}_1}$ whose density has been subtracted to the overall continuous distribution.

Successively, at t_2, analogous local signals simultaneously stimulate each aggregate in three different points (i.e., $\mathbf{q}_2 = (300\,\mu\mathrm{m}, 320\,\mu\mathrm{m})$, $\mathbf{q}_3 = (309.4\,\mu\mathrm{m}, 107, 2\,\mu\mathrm{m})$ and $\mathbf{q}_4 = (151.2\,\mu\mathrm{m}, 225.4\,\mu\mathrm{m})$ in the case of setting 1, $\mathbf{q}_2 = (150\,\mu\mathrm{m}, 160\,\mu\mathrm{m})$, $\mathbf{q}_3 = (154.9\,\mu\mathrm{m}, 53.6\,\mu\mathrm{m})$ and $\mathbf{q}_4 = (75.6\,\mu\mathrm{m}, 112.7\,\mu\mathrm{m})$ in the case of setting 2, and $\mathbf{q}_2 = (144.2\,\mu\mathrm{m}, 152.2\,\mu\mathrm{m})$, $\mathbf{q}_3 = (148.2\,\mu\mathrm{m}, 70.5\,\mu\mathrm{m})$ and $\mathbf{q}_4 = (84.2\,\mu\mathrm{m}, 114.1\,\mu\mathrm{m})$ in the case of setting 3), see Fig. 3. In the case of the initial configuration 3, cell phenotypic transitions are observed in all the three stimulated points. For settings 1 and 2, cell activation actually occurs only in $\mathbf{q}_3$ and in $\mathbf{q}_4$: in both cases, the mass density distributed over the support of $w_{\mathbf{q}_2}$ is in fact not sufficient to constitute a localized differentiated individual.

Finally, we further assume that a localized cell maintains its activated status only for a limited period: after that, it returns to a quiescent/deactivated condition. At t_3, for all settings, the firstly activated cell located in $\mathbf{q}_1$ is assumed to turn back to the quiescent state as its period of differentiation has terminated: therefore, in all system configurations, the initial mass distribution is locally recovered, see Fig. 3. It is useful to remark that, in these test simulations, both the times and the points of the above-described cell phenotypic transitions have been randomly chosen.

3 Modelling the interaction dynamics

A key feature of the proposed hybrid modelling framework is the possibility to define a proper evolution law for each subpopulation according to its specific behavior. In this respect, in this section, we enrich the above-proposed procedure with proper cell migratory dynamics and proliferation/death processes.

Let us consider a biological system composed by two clones of the same cell lineage, whose biophysical properties and behaviour justify the convenience of a hybrid representation of the system (see Eq. (3)). In particular, referring to the above-considerations, we adopt a localized/pointwise description for specialized/differentiated cells, and prefer a distributed representation of the rest of the system, i.e., for unspecialized/undifferentated individuals. In this respect, the set of localized individuals evolves following a system of first order ODEs, while the dynamics of the distributed part of the aggregate is regulated by the local form of a mass balance equation:

$$\begin{cases} \dfrac{d\mathbf{x}_j(t)}{dt} = \mathbf{v}_L(\mathbf{x}_j(t)), \quad j = 1, \ldots, N_L(t), \\[2mm] \dfrac{\partial \rho(t, \mathbf{y})}{\partial t} + \nabla \cdot (\rho(t, \mathbf{y})\, \mathbf{v}_D(t, \mathbf{y})) = \Gamma(t, \mathbf{y}), \end{cases} \tag{13}$$

where $\mathbf{x}_j$ and ρ are defined in Eq. (3), and $\mathbf{v}_L$ and $\mathbf{v}_D$ are the velocity of the two cell clones, respectively. The term Γ is the proliferation/apoptosis rate of the distributed part of the aggregate. As already said, possible duplication/death

processes of localized individuals can be implemented by defining a proper evolution law for their number N_L. In Eq. (13), we have assumed that the velocity of moving individuals and not their acceleration is proportional to the sensed forces: this is the so-called *overdamped force-velocity assumption*, that holds for extremely viscous regimes, such as biological environments (see [30] for a detailed comment). Then, assuming that, in general, cell dynamics are established by both a directional motion and by intercellular interactions, in Eq. (13), we set

$$
\begin{cases}
\mathbf{v}_L(\mathbf{x}_j(t)) = \widehat{\mathbf{v}}_L(\mathbf{x}_j(t)) + \displaystyle\sum_{i=1}^{N_L} \overline{m}\, \mathbf{K}^{LL}(\mathbf{x}_i(t) - \mathbf{x}_j(t)) + \\
\qquad\qquad\qquad\qquad\qquad + \displaystyle\int_\Omega \mathbf{K}^{LD}(\boldsymbol{\xi} - \mathbf{x}_j(t))\rho(t,\boldsymbol{\xi})\, d\boldsymbol{\xi}; \\
\mathbf{v}_D(\mathbf{y}) = \widehat{\mathbf{v}}_D(\mathbf{y}) + \displaystyle\sum_{i=1}^{N_L} \overline{m}\, \mathbf{K}^{DL}(\mathbf{x}_i(t) - \mathbf{y}) + \displaystyle\int_\Omega \mathbf{K}^{DD}(\boldsymbol{\xi} - \mathbf{y})\rho(t,\boldsymbol{\xi})\, d\boldsymbol{\xi}.
\end{cases}
$$
$$(14)$$

Specifically, the functions $\widehat{\mathbf{v}}_L : \mathbb{R}^2 \mapsto \mathbb{R}^2$ and $\widehat{\mathbf{v}}_D : \mathbb{R}^2 \mapsto \mathbb{R}^2$ implement the directional contribution to cell velocity, which may arise from environmental determinants, e.g., the local concentration/stiffness of the extracellular matrix components (haptotaxis/durotaxis) or on the spatial distribution of some diffusive chemicals (chemotaxis).

The sum and integral terms in Eq. (14) represent instead the velocity components due to direct intercellular interactions. In this respect, the kernels $\mathbf{K}^{\alpha\beta} : \mathbb{R}^2 \mapsto \mathbb{R}^2$ (where $\alpha, \beta, \in \{L, D\}$) define how a localized cell (if $\alpha = L$) or a distributed infinitesimal mass (if $\alpha = D$) is influenced in its dynamics by a specialized cell (if $\beta = L$) or by an infinitesimal unspecialized mass (if $\beta = D$). In this respect, there exist several possibilities to specify the form of $\mathbf{K}^{\alpha\beta}$. However, hereafter we employ the following set of assumptions: (i) intercellular interactions involve cell-cell adhesion, due to the expression of cadherin adhesive molecules, and cell-cell repulsion, which reproduces cell resistance to compression; (ii) the resulting velocity components give an effect along the direction connecting the interacting elements, depending for instance on their relative position; (iii) intercellular interactions are isotropic and occur only within limited cell neighborhoods (metric interactions). In particular, repulsive interactions activate only within a cell repulsive neighborhood defined by a mean cell diameter, d_r, that determines the minimal space occupied by a cell (which is consistently equal to $2\,r_c$, where r_c has been defined in Eq. (5)). On the opposite intercellular adhesive forces occurs over a cell neighborhood defined by the maximal distance reached by cell mobile adhesive structures (i.e., filopodia and pseudopodia), identified by d_a (as represented in Fig. 4). In this respect, it is consistent to assume $d_\mathrm{a} > d_\mathrm{r}$, as wandering cells are able to extends membrane protrusions sufficiently far from their main body. The hypothesis of isotropy applies to cells characterized by a homogeneous distri-

bution of receptors or adhesive molecules all over their membrane. Summing up, defining as $F_r^{\alpha\beta}$ cell intrinsic resistances to compression and as $F_a^{\alpha\beta}$ the measures of the amount of expressed and activated cadherins, we can write:

$$\mathbf{K}^{\alpha\beta}(|\mathbf{r}|) = \mathcal{K}^{\alpha\beta}(|\mathbf{r}|)\,\frac{\mathbf{r}}{|\mathbf{r}|} = \mathcal{K}^{\alpha\beta}[d_r, F_r^{\alpha\beta}, d_a, F_a^{\alpha\beta}](|\mathbf{r}|)\,\frac{\mathbf{r}}{|\mathbf{r}|}. \qquad (15)$$

In this respect, it is worth to note that the interaction distances are set to be independent from the specific cell phenotype (i.e., d_a and d_r are in common for all cell subpopulations taken into account). The strengths of the interacting forces may instead vary according to the type of interacting elements. Analogous interaction terms have been introduced in [12] and [13] where a hybrid discrete/continuous representation of a two-population system is obtained by employing a measure-theoretic approach. Other examples of non-local integro-differential models to describe selected dynamics of heterogeneous cell aggregates are proposed in [3], [4] and [26]. In particular, in [3] and [4], cell movement is determined by adhesive forces: using a continuous approach, the authors represent cell adhesion with an integral term over a sensing region, which is defined as the area over which a cell can sense the surrounding environment. In [26], instead, the dynamics of both homogeneous and heterogeneous aggregates are given by a non-local PDE model which includes both attracting and repelling signals directly transmitted over different interaction ranges.

We then turn to apply the resulting complete model to a couple of biological phenomena: i) selected phenomenologies of the avascular growth and invasion of a solid tumor spheroid and ii) the stage of the formation of the zebrafish posterior lateral line. It is worth to note that the aim of the following numerical realizations is to show the advantages of the proposed modelling approach in realistic biological contexts, however without claiming to be exhaustive in the description of the phenomena of interest.

3.1 Avascular tumor growth and invasion

The evolution of a tumor spheroid can be characterized by tumor finger formation or spreading of metastasis (cell scattering). In both cases, the malignant mass is formed by two clones of cancer cells, that have equal geometrical dimensions but distinct behaviour: a differentiated/metastic group of individuals (hereafter labeled by "M"), activated by a given amount of growth factors, and a quiescent mass ("Q"). The former cell phenotype has reduced adhesive interactions and an increased migratory ability (in particular, high chemotactic strength). On the contrary, the latter cell clone has significant adhesiveness and enhanced proliferation/death cycles, but no migratory ability. Taking these considerations into account, it is natural to use a pointwise description for metastatic individuals and a distributed representation for the rest of the tumor mass (defined by the mass density ρ). In this respect, the
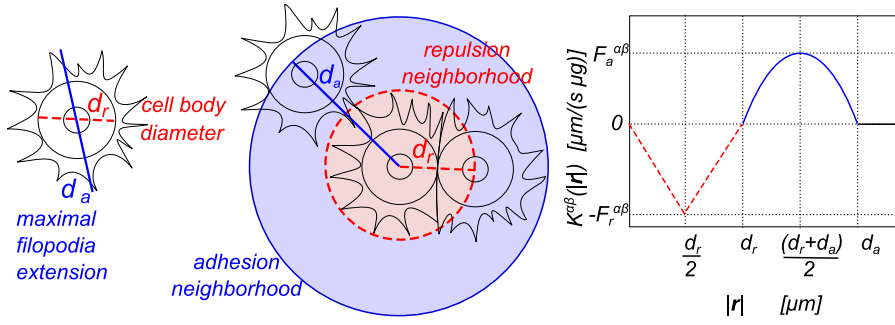
Fig. 4 Left panel: Sketch of cell body. d_r represents the mean cell diameter (dashed line), d_a is the maximum distances reached by cell adhesive structures (solid line). Central panel: Cell interaction neighborhoods. Repulsive interactions occur between cells whose relative distance is less then d_r, i.e., less than a mean cell diameter (dashed circle). Adhesive interactions instead occur within a cell relative distance d_a which is possibly the maximum extension of cell adhesive structures (solid circle). Right panel: Plot of the proposed interaction kernel. d_r, d_a are the repulsive and attractive radii, respectively, and $F_r^{\alpha\beta}$, $F_a^{\alpha\beta}$ the strengths of the corresponding interactions occurring between cell phenotype α and β.

dynamics of the set of activated/localized individuals and the the distributed part of the aggregate is given by Eq. (13) and (14), with $L = M$ and $D = Q$.

Entering more in details, in this context, a plausible law for duplication/apoptosis processes of the quiescent part of the tumor is given by

$$\Gamma(t, \mathbf{y}) = \left[\gamma \left(1 - \frac{\rho(t, \mathbf{y})}{\rho_{\max}} \right) - \delta \right] \rho(t, \mathbf{y}), \tag{16}$$

where γ and δ are the proliferation and death rate, respectively, while $\rho_{\max} = 2 w_{\max} = 2 \max_{\mathbf{y}} \{ w_{(\cdot)}(\mathbf{y}) \} = 2 \cdot 10^{-5} \ \mu g/(\mu m)^2$ is a maximum admissible value for the cell mass density. In particular, by assuming logistic growth and constant death rate for the quiescent mass, we are including in the model both a contact-inhibited cell proliferation and a natural cell apoptosis.

The directional velocity component is active only for metastatic individuals (i.e., $\widehat{\mathbf{v}}_Q \equiv 0$) and implements the chemotactic velocity as follows

$$\widehat{\mathbf{v}}_M(\mathbf{x}_j(t)) = \min\{ k_0 |\nabla c(t, \mathbf{x}_j(t))|; \ \mathbf{v}_{\max} \} \frac{\nabla c(t, \mathbf{x}_j(t))}{|\nabla c(t, \mathbf{x}_j(t))|}, \tag{17}$$

where c is the concentration of the molecular chemotactic substance (see Eq. (19) below), $k_0 = 4 \cdot 10^9 \ \mu m^2/(\mu M \, s)$ is the cell chemical response and $\mathbf{v}_{\max} = 0.0025 \ \mu m/s$ is a maximum admissible speed, taken from the biological literature [1].

Keeping in mind the assumption that the cell subpopulations forming the tumor are two clones of the same cell lineage, that have equal physical properties but different behaviours, we set for both $d_r = 30 \ \mu m$ and $d_a = 60 \ \mu m$, which are coherent with the experimental measurements on tumor (refer to [5] for gliomas and to [27] for ovarian cancer spheroids). Although there are several options to specify the form of interactions kernels $\mathbf{K}^{\alpha\beta}$ (where $\alpha, \beta, \in \{M, Q\}$),

assuming, as already said, repulsive/adhesive metric isotropic interactions (cf. Eq. (15)), we set

$$
\mathcal{K}^{\alpha\beta}(\mathbf{r}) =
\begin{cases}
-\dfrac{2F_{\mathrm{r}}^{\alpha\beta}|\mathbf{r}|}{d_{\mathrm{r}}} & \text{if } |\mathbf{r}| < \dfrac{d_{\mathrm{r}}}{2}; \\[2ex]
2F_{\mathrm{r}}^{\alpha\beta}\left(\dfrac{|\mathbf{r}|}{d_{\mathrm{r}}} - 1\right) & \text{if } \dfrac{d_{\mathrm{r}}}{2} \leq |\mathbf{r}| < d_{\mathrm{r}}; \\[2ex]
-\dfrac{4F_{\mathrm{a}}^{\alpha\beta}}{(d_{\mathrm{a}} - d_{\mathrm{r}})^2}\left(|\mathbf{r}| - d_{\mathrm{r}}\right)\left(|\mathbf{r}| - d_{\mathrm{a}}\right) & \text{if } d_{\mathrm{r}} \leq |\mathbf{r}| < d_{\mathrm{a}}; \\[2ex]
0 & \text{otherwise,}
\end{cases}
\tag{18}
$$

see Fig. 4 and refer to [12]. The specific values both of the intercellular adhesive/repulsive strengths and of the quiescent cell proliferation/death rates, whose units are $\mu\mathrm{m}/(\mu\mathrm{g\ s})$ and s^{-1}, respectively, have been empirically estimated, after a number of trial simulations and in accordance with reasonable biological considerations. In this respect, proper values of homotypic (i.e., between elements of the same subpopulation) and heterotypic (i.e., between elements belonging to different subpopulations) repulsion strengths and of homotypic adhesive strengths are $F_{\mathrm{r}}^{\mathrm{MM}} = F_{\mathrm{r}}^{\mathrm{QQ}} = 10^{-4}\ \mu\mathrm{m}/(\mu\mathrm{g\,s})$, $F_{\mathrm{r}}^{\mathrm{MQ}} = F_{\mathrm{r}}^{\mathrm{QQ}} = 10^{-5}\ \mu\mathrm{m}/(\mu\mathrm{g\,s})$, $F_{\mathrm{a}}^{\mathrm{MM}} = 0\ \mu\mathrm{m}/(\mu\mathrm{g\,s})$ and $F_{\mathrm{a}}^{\mathrm{QQ}} = 2.5 \cdot 10^{-5}\ \mu\mathrm{m}/(\mu\mathrm{g\,s})$. The heterotypic adhesive strengths and the proliferation/death rates of the quiescent cell lineage will be instead specified in the following, according to the selected phenomenology of avascular growth of a solid tumour. For reader convenience, all the parameter values are listed in Tables 1, 2 and 3.

The evolution of the chemical which, as seen, behaves both as an activator for the quiescent tumor mass and as a chemotactic cue for the already-metastatic individuals is regulated by the following standard reaction-diffusion equation

$$
\begin{cases}
\dfrac{\partial c}{\partial t}(t, \mathbf{y}) = D\Delta c(t, \mathbf{y}) - \epsilon c(t, \mathbf{y}), & \mathbf{y} \in \Omega; \\[2ex]
c = c_0, & \mathbf{y} \in \partial\Omega;
\end{cases}
\tag{19}
$$

where $D = 10\ \mu\mathrm{m}^2/\mathrm{s}$ is the constant and homogeneous diffusion coefficient, $\epsilon = 1.8 \cdot 10^{-4}\ \mathrm{s}^{-1}$ is the decay rate and $c_0 = 2.17 \cdot 10^{-4}\ \mu\mathrm{M}$ is the amount of chemical prescribed over the whole edge of the computational domain Ω. Such a boundary condition implements a constant supply of chemical factors from the host tissue to the tumor. It is also useful to remark that the kinetics law (19) will hold for the simulations proposed both in Section 3.1.1 and in Section 3.1.2. The cell activation threshold is then set equal to $c_s = 1.0 \cdot 10^{-8}\ \mu\mathrm{M}$, i.e., the cell phenotypic transition described in Eq. (8) is actually stimulated in a point $\mathbf{x}_s \in \Omega$ if $c(t, \mathbf{x}_s) > c_s$. To avoid the formation of quasi or completely overlapped metastatic cells, we assume that a cell activation in $\mathbf{x}_s$ inhibits further cell differentiation over a ball centered in $\mathbf{x}_s$ with radius r_{inh}. Comparable regulatory mechanisms of phenotypic transitions are present

Table 1 Model parameters used for all simulations of tumor growth.

Param.	Description	Value [Units]
Ω	computational domain	800×800 [μm^2]
	grid size	4 [μm]
	initial amount of quiescent cells within the tumor spheroid	288
	initial radius of the tumor spheroid	134 [μm]
r_c	mean cell radius	15 [μm]
h_c	mean cell height	10 [μm]
$\overline{m}$	mean cell mass	$1.8 \cdot 10^{-3}$ [μg]
$v_{\max}$	maximum admissible cell speed	0.0025 [μm/s]
k_0	chemotactic coefficient	$4 \cdot 10^9$ [μm^2/(μM s)]
$d_{\rm r}$	intercellular repulsion radius	30 [μm]
$d_{\rm a}$	intercellular adhesion radius	60 [μm]
$F_{\rm r}^{\rm MM}$	homotypic repulsion between metastatic cells	10^{-4} [μm/(μg s)]
$F_{\rm r}^{\rm MQ}$	heterotypic intercellular repulsion	10^{-5} [μm/(μg s)]
$F_{\rm r}^{\rm QM}$	heterotypic intercellular repulsion	10^{-5} [μm/(μg s)]
$F_{\rm r}^{\rm QQ}$	homotypic repulsion between quiescent cells	10^{-4} [μm/(μg s)]
$F_{\rm a}^{\rm MM}$	homotypic adhesion between metastatic cells	0 [μm/(μg s)]
$F_{\rm a}^{\rm QQ}$	homotypic adhesion between quiescent cells	$2.5 \cdot 10^{-5}$ [μm/(μg s)]
D	chemical diffusion coefficient	10 [μm^2/s]
ϵ	chemical decay rate	$1.8 \cdot 10^{-4}$ [s^{-1}]
c_0	chemical concentration at $\partial\Omega$	$2.17 \cdot 10^{-4}$ [μM]
c_s	chemical threshold for cell activation	10^{-8} [μM]

in a wide range of processes, such as physio-pathological vascular progressions (it is the so-called *Delta-Notch signalling pathway*).

Given a domain $\Omega = [0, 800] \times [0, 800]$ μm^2 (compartmentalized for computational purposes with grid elements of size 4.0 μm), in all realizations, we start with a completely quiescent tumor spheroid (i.e., $\mathbf{X}(0) = \emptyset$ and $N_L(0) = 0$), whose mass density is inhomogeneously distributed over a round compact of radius 134 μm to have an overall amount of $M_D(0) = 288\overline{m}$ (i.e., the mass of 288 cells). The initial condition of the tumor, as well as the specific estimates of relevant model parameters, will be specified for each set of simulations.

3.1.1 Tumor finger formation

We first assume that the initial distribution of the malignant mass consists of a set of 288 overlapping bell functions (i.e., which corresponds to 288 quiescent cells). They are arranged with same mutual distance as in the case of the setting 2 shown in Fig. 3 (i.e., $|\mathbf{x}_h - \mathbf{x}_k| = 15$ μm $= r_c$, where $\mathbf{x}_h$ and $\mathbf{x}_k$ define the centers of any pair of first-nearest neighbor bell functions). The quiescent cells proliferation and death rates in Eq. (16) are set equal to $\gamma = 10^{-4}$ s^{-1} and $\delta = 10^{-5}$ s^{-1}, respectively, while the heterotypic intercellular adhesive strength are estimated in $F_{\rm a}^{\rm MQ} = 10^{-4}$ μm/(μg s) and $F_{\rm a}^{\rm QM} = 10^{-3}$ μm/(μg s). In particular, by setting $F_{\rm a}^{\rm MQ} < F_{\rm a}^{\rm QM}$, we assume that heterotypic adhesions affect the dynamics of the involved infinitesimal quiescent/distributed mass, rather
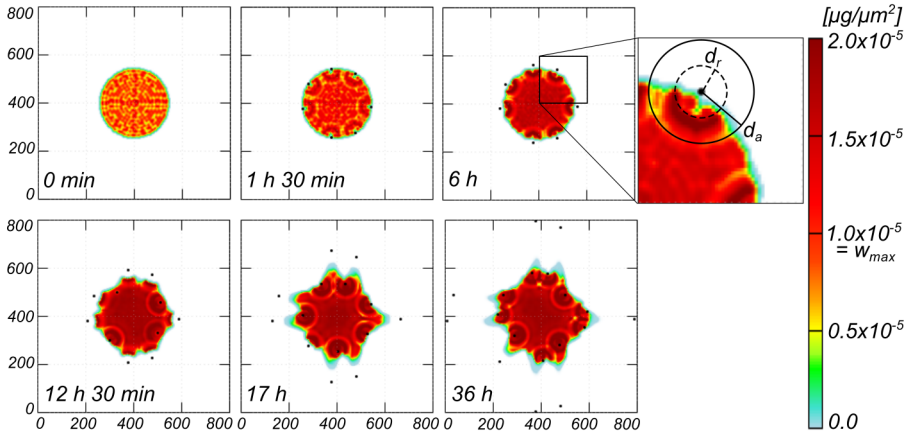
Fig. 5 Avascular growth of a tumor spheroid with finger formation. Top panels: As the chemical diffusive front reaches the spheroid, seven single cells differentiate at the external rim of the malignant mass. Differentiated individuals start to invade the host tissue, followed by finger-like structures emerging from the quiescent malignant mass. Simultaneously, the inner part of the spheroid reaches a stable quasi-uniform configuration. Bottom panels: When the firstly activated cells separate from the original tumor (around 12 hours), a second differentiation occurs in the gaps between successive fingers-like structures. Heterotypic interactions involving the such a newly activated cells help finger elongation, as the firstly activated individuals are dispersed in the extracellular host.

than the velocity of the interacting matastatic/localized cell. Furthermore, we assume that chemical-induced phenotypic differentiations possibly occur only in a 30 μm-wide external rim of the tumor, i.e., from a computational point of view, if $\mathbf{x}_s$ falls within this area. Such a spatial restriction is coherent with experimental observations, which prove that active and highly metabolic individuals are mainly present in the outer regions of malignant masses, whereas their interior bands are typically filled by quiescent cells, see [7] and [8] and references therein.

First, due to inner interactions and proliferation/death processes, the quiescent malignant mass slightly adjusts its initial configuration and grows (see Fig. 5). Then, the chemical diffusive front reaches the spheroid and locally exceeds the critical threshold of c_s. Suddenly, a differentiation (with the corresponding switch in the mathematical descriptive instances) occurs on the external rim of the malignant mass: in particular, seven cells activate, whose distance satisfies the above-described (i.e., in the paragraph just below Eq. (19)) mechanism of spatial inhibition of differentiation, with $r_{\mathrm{inh}} = 100$ μm. As represented in the zoom view of Fig. 5, bulks of higher density cluster in the proximity of the location of the activated individual (see the dark red density): this phenomenology is due to the fact that the quiescent mass is attracted within the adhesive neighborhood of each differentiated cell, however it is repelled as soon as it approaches the repulsive regions: as a consequence, a circular ring of higher cell quiescent mass stabilized around the activated elements. As reproduced in Fig. 5 (top panels), the activated malignant in-

Table 2 Model parameters which characterize for the simulation of tumor finger formation.

Param.	Description	Value [Units]
F_a^{MQ}	heterotypic intercellular adhesion	10^{-4} $[\mu m/(\mu g\,s)]$
F_a^{QM}	heterotypic intercellular adhesion	10^{-3} $[\mu m/(\mu g\,s)]$
γ	proliferation rate	10^{-4} $[s^{-1}]$
δ	death rate	10^{-5} $[s^{-1}]$
r_{inh}	spatial inhibition radius	100 $[\mu m]$

dividuals then chemotactically react to the molecular substance gradients, thereby starting to crawl in the extracellular host toward the nearest edge of the domain. Due to the chemotactic motion of localized cells, as well as to the heterotypic adhesive interactions and the duplication processes of quiescent cells, small finger structures, formed by inactivated individuals, begin to extend from the external rim of the tumor mass beside each leader individual. At the same time, the duplication/apoptosis processes and the homotypic interactions of the quiescent part of the tumor lead the inner core of the spheroid (i.e., where quiescent cells are not able to differentiate) to reach and maintain a quasi-uniform distribution. As shown in Fig. 5 (bottom-left panel), once the leader cells separate enough from the rest of the tumor, a second phase of differentiation occurs at the border of the tumor: this is due to the fact that the distance between the firstly activated cells and the edge of the spheroid is greater than r_{inh}, so that further phenotypic transitions are no longer inhibited. Interestingly, as shown in Fig. 5 (bottom panels), the elongation of the finger-like structures is then no longer guided by the firstly formed leader cells, which are now dispersed in the extracellular host, but by the secondly activated individuals. It is useful to notice that fingering dynamics arises only from specific ranges of model parameters: too low heterotypic adhesiveness (as well as high enough values of the chemotactic strength) would result in the immediate dispersion of activated cells without any deformation of the circular mass (not shown); a too high exogenous adhesiveness (as well as too low chemotactic response) would instead result in the absorption of the differentiated individuals within the bulk of the tumor (not shown). Further, too low proliferation/death rates would results in a decrease of the frequency of cell activation, prevented by a non sufficient amount of mass, with a consequent reduction of the number and the thickness of formed fingers.

The phenomenon of fingering characterizes several types of solid tumors. In particular, malignant masses with an unstable fingered morphology are more aggressive and hard to be treated than smoother ones: in fact, even if their invasive depth is typically limited, they are difficult to be surgically removed. Such dynamics have been reproduced by several modelling approaches. First, in [35], a suitable version of the cellular Potts model captures fingering extension from the edge of a planar tumor mass as a consequence of a balance between intercellular adhesiveness and cell haptotactic response to non-diffusive substrate gradients (i.e., resembling different concentration of matrix bound
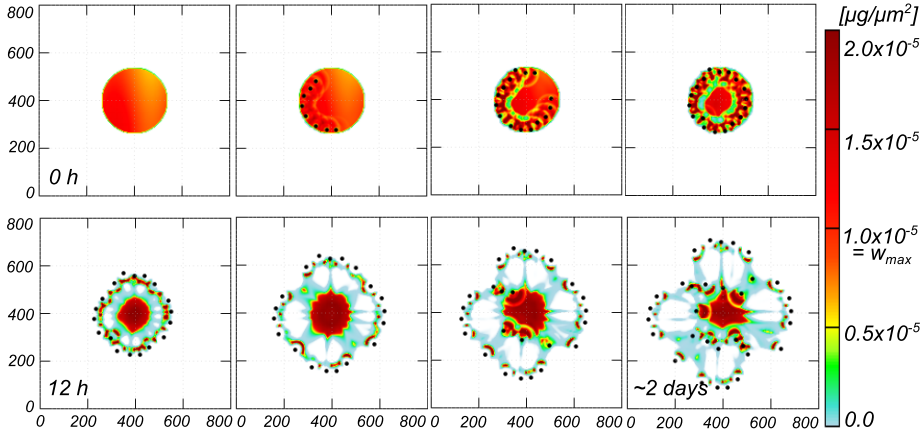
Fig. 6 Avascular growth of a tumor spheroid with spreading metastasis. Due to an extracellular chemical stimulus, cell differentiations occur in the external rim of the spheroid, starting from the densest part of the tumor. Heterotypic interactions then force quiescent mass in the external part of the tumor to cluster around the nearest activated cell (top panels). Differentiated cells then start to chemotactically react to the molecular substance gradient, so that an invading rim of metastatic cells expands in the host followed by quiescent clusters. Concomitantly, the bulk of the original spheroid continues to proliferate, thereby becoming a source for a possible *in situ* tumor relapse (bottom panels).

proteins such as fibronectin and laminin) without the presence of cell proliferation. Cell duplication, as long as adhesion, autocrine and paracrine growth stimulation and stromal destruction, is instead critical to have multicellular tongue formation in a cellular automaton model for tumor growth [32]. In [38], fingering phenomena are instead captured by a diffusive interface continuum model of multispecies tumor growth. The simulations presented therein show such a complex structures arise from a diffusional instability, which leads to the creation of buds elongating into protruding tumor tongues. Finally, in [2], a hybrid discrete-continuum (HDC) model, in which cells are treated as discrete stochastic variables and the microenvironmental parameters as deterministic concentrations, analyzes tumor morphology and phenotypic evolution under different pressure conditions. In particular, invasive masses characterized by fingering margins, which are dominated by few clones with aggressive traits, are observed in harsh conditions of the tumor microenvironment (e.g., hypoxia).

3.1.2 Spread of metastasis

We then turn to apply the model to a tumour spheroid characterized by pathological overgrowth (with the consequent disruption of the physiological regulatory mechanisms of contact inhibition of growth) and scattering phenotype. From a modelling point of view this amounts in reducing the area interested by the above-described spatial inhibition of differentiation (i.e., reducing r_{inh} to $40~\mu$m), in increasing both the proliferation/death rates of the quiescent mass

(i.e., setting $\gamma = 2 \cdot 10^{-4}$ and $\delta = 2 \cdot 10^{-5}$, respectively), and finally in modifying the heterotypic adhesive strengths (i.e., reducing F_a^{MQ} to 10^{-6} μm/(μg s) and increasing F_a^{QM} to $5 \cdot 10^{-3}$ μm/(μg s)). With respect to the previous case, the latter assumption means that the quiescent part of the tumour experiences a stronger adhesion to the localized cells, which are instead characterized by an increased attitude to move according to their directional velocity. In this case, we start with a round and completely quiescent spheroid whose mass density is heterogenous and given by

$$\rho(0, \mathbf{y}) = 0.8 \cdot 10^{-5} + 0.15 \cdot 10^{-5} \left(\cos\left(\frac{y_1}{50}\right) + \sin\left(\frac{y_2}{150}\right) \right) \qquad (20)$$

for any $\mathbf{y} = (y_1, y_2)$ within the ball centered in (400 μm, 400 μm) with radius equal to 134 μm, as reproduced in Fig. 6 (top-left panel). This means that, roughly speaking, cell density is higher on the left then on the right side of the spheroid. The overall amount of cellular mass corresponds to 288 individuals.

As in the previous case, homotypic interactions and proliferation/death processes of the quiescent part of the tumor lead to slight adjustments of the initial configuration. As before, once the chemical reaches the malignant mass and locally exceeds the critical threshold of c_s, a differentiation occurs on the external rim of the spheroid. However, this time, due to the heterogeneous distribution of the mass of the aggregate, cell phenotypic differentiation starts from the densest part of the tumor edge. In fact, only in such a region of the colony there is initially an amount of cell mass sufficient to have phenotypic transitions. As reported in Fig. 6 (top panels), the inclusion both of high proliferation/death rates and of the relaxation in the spatial inhibitory mechanism of cell differentiation results in a significant growth of the tumor mass, and in the consequent dramatic activation of a high number of aggressive cells, also in the other parts of the spheroid edge. Due to the increased F_a^{QM}, inactivated individuals in the external rim of the spheroid suddenly detach from the rest of the malignant mass and cluster, at a distance equal to d_r, around the activated cells. Concomitantly, differentiated individuals, being characterized by reduced adhesive interactions F_a^{MQ}, spread away followed by the clustered quiescent mass (see Fig. 6 (bottom-left panels)). As a results, we observe an invading rim of tumor that expands in the host, while the remaining quiescent malignant core goes on proliferating and possibly differentiating, thereby constituting a source for a further *in situ* tumor relapse (see Fig. 6 (bottom-right panels)).

Regarding the second phenotype of the tumor growth reproduced by our model, it is useful to notice that the dispersion of a number of shed activated cells or of small clusters of quiescent cells following activated individuals strongly increase the aggressiveness of the disease. Single high motile malignant cells are in fact difficult to be clinically detected and have the greatest potential to invade the host and further metastasize, as they are able to evade destruction by the immune system and to subsequently enter the host bloodstream or lymphatics, extravasate at a distant site, and establish secondary colonies with devastating consequences for the wellbeing of the patient, as the

Table 3 Model parameters which characterize for the simulation of spreading metastasis.

Param.	Description	Value [Units]
F_a^{MQ}	heterotypic intercellular adhesion	10^{-6} $[\mu m/(\mu g\,s)]$
F_a^{QM}	heterotypic intercellular adhesion	$5 \cdot 10^{-3}$ $[\mu m/(\mu g\,s)]$
γ	proliferation rate	$2 \cdot 10^{-4}$ $[s^{-1}]$
δ	death rate	$2 \cdot 10^{-5}$ $[s^{-1}]$
r_{inh}	spatial inhibition radius	40 $[\mu m]$

likelihood of success of therapeutic interventions strongly decreases. In this respect, as a further support of our considerations, a wide range of experimental studies have recently demonstrated that the down-regulation of cadherin molecules (at the basis of the scattering of the activated cells) is implicated in a variety of metastatic cancers [10], [11], [34]. In particular, glioma cell lines with low N-cadherin expressions (leading to low adhesivity) have been observed to aggressively invade matrix gels, whereas the same populations with a high N-cadherin activity have been instead shown to grow slower and to expand less significantly in the host tissues [19]. Finally, cell differentiation and subsequent dissociation can be triggered in neoplastic cells of epithelial origin by several growth factor, for example the hepatocyte growth factors [14], [36]. It is finally useful to remark that the evolution of the malignant mass captured in our simulations reproduces only the avascular stage of tumor growth (i.e., before the angiogenic transition necessary for the disease to go on survive): our results are however consistent with experimental outcomes, i.e., in case of spheroids of ovarian [8], [31] or breast [17] carcinomas plated in spinner cultures, and of gliomas, both embedded *in vitro* in collagenous gels [22], [33] and implanted *in vivo* in mice [9].

3.2 First stage of zebrafish posterior lateral line formation

We finally employ our modelling framework to describe selected features of the initial formation of the zebrafish posterior lateral line (pLL), which constitutes an interesting system widely used to study cell differentiation and collective migration (see also [15] and references therein). Moreover, from a modelling point of view, this is an interesting application of the proposed approach, as it requires the extension of the modelling framework to the case of three different clones of the same cell lineage. Furthermore, in this context, the cell phenotypic transitions imply the use of the representation switch defined in Eq. (6), i.e., from a localized/pointwise to a distributed cell description, whose underlying mechanisms have been previously shown in the test simulation of Section 2.

Entering in more details, the zebrafish has a set of mechanosensory hair cell organs, the neuromasts, which are distributed in a stereotyped pattern over the body surface, the tail, and the caudal fin (see Fig. 1 in [18]). The pLL

is a part of such a sensory network, i.e., the lateral line, which has the function to detect water displacements and vibrations, thereby allowing the animal to perform several fundamental activities, such as prey detection, predator avoidance, and sexual courtship. During development, the zebrafish pLL consists of a *primordium*, a proto-organ formed by a group of epithelial cells with mesenchymal determinants, such as loss of apicobasal polarity, reduced expression of epithelial markers and of tight junction (i.e., adhesive) proteins and increased number of dynamic filopodia. These pseudo-mesenchymal (pM) individuals, hereafter labeled by "M", are situated behind the ear and are able to organize into polarized rosettes, each corresponding to a hair cell organ progenitors, termed proneuromast. In particular, a single anteriorly positioned rosette first forms; then, over the next few hours, additional rosettes are sequentially added to the posterior. Once three or four rosettes have formed, the overall primordium begins to migrate toward the tail. During this motion, proneuromasts are deposited along the body of the animal, according to the stereotyped pattern that will characterize the mature pLL of the zebrafish. Over the course of migration, the onset of a neuromast deposition at the anterior edge correlates with the generation of a new rosette near the posterior zone, leading to cyclical dynamics.

Following the biological observations presented in [25], the formation of each rosette can be schematized as follows: specific sdf-1 genetic and biochemical pathways (triggered by overexpression of fgf receptors) select a few of the pM cells forming the primordium, which are sufficiently far one to each other. Such differentiated individuals (hereafter identified by "M$^+$") then induce the surrounding cells (hereafter labeled by type "E") to acquire a fully epithelial fate, i.e., increment in adhesiveness and inhibition of motility structures. This change in cell state has been termed *pseudo* (or *inverse*) *epithelial-to-mesenchymal transition* (P-EMT or I-EMT).

We here aim to reproduce the main steps of the formation of the first three rosettes within the primordium body: in this respect, our model includes the mechanisms of cell differentiation, phenotypic transition, intercellular adhesive/repulsive dynamics, but not productive directional migration (which, as seen, characterizes a second phase of the pLL development) and cell proliferation/death mechanisms. Within our modelling environment, we opt to use a pointwise representation for both clones of pseudo-mesenchymal cells (M and M$^+$) and a distributed description for the mass of fully epithelial individuals (E). This is in accordance with the previous sections, where a localized mathematical descriptive instance has been consistently proposed for activated less adhering cells, i.e., characterized by a mesenchymal/metastatic phenotype. At any given time t, the hybrid representation of the primordium is therefore

Table 4 Model parameters used for the simulation of zebrafish pLL formation.

Param.	Description	Value [Units]
Ω	computational domain	$200 \times 50 \ [\mu m^2]$
	grid size	$1 \ [\mu m]$
r_c	mean cell radius	$5 \ [\mu m]$
h_c	mean cell height	$10 \ [\mu m]$
$\overline{m}$	mean cell mass	$0.2 \cdot 10^{-3} \ [\mu g]$
d_{r}	intercellular repulsion radius	$10 \ [\mu m]$
d_{a}	intercellular adhesion radius	$15 \ [\mu m]$
$F_{\mathrm{r}}^{\mathrm{MM}}$	homotypic repulsion between pseudo-mesenchymal non-activated cells	$10^{-4} \ [\mu m/\mu g \, s]$
$F_{\mathrm{a}}^{\mathrm{MM}}$	homotypic adhesion between pseudo-mesenchymal non-activated cells	$10^{-5} \ [\mu m/\mu g \, s]$
$F_{\mathrm{r}}^{\mathrm{MM}^+}$	heterotypic intercellular repulsion	$10^{-4} \ [\mu m/\mu g \, s]$
$F_{\mathrm{a}}^{\mathrm{MM}^+}$	heterotypic intercellular adhesion	$10^{-5} \ [\mu m/\mu g \, s]$
$F_{\mathrm{r}}^{\mathrm{ME}}$	heterotypic intercellular repulsion	$10^{-3} \ [\mu m/\mu g \, s]$
$F_{\mathrm{a}}^{\mathrm{ME}}$	heterotypic intercellular adhesion	$10^{-4} \ [\mu m/\mu g \, s]$
$F_{\mathrm{r}}^{\mathrm{M}^+\mathrm{E}}$	heterotypic intercellular repulsion	$10^{-3} \ [\mu m/\mu g \, s]$
$F_{\mathrm{a}}^{\mathrm{M}^+\mathrm{E}}$	heterotypic intercellular adhesion	$10^{-4} \ [\mu m/\mu g \, s]$
$F_{\mathrm{r}}^{\mathrm{M}^+\mathrm{M}^+}$	homotypic repulsion between pseudo-mesenchymal activated cells	$10^{-4} \ [\mu m/\mu g \, s]$
$F_{\mathrm{a}}^{\mathrm{M}^+\mathrm{M}^+}$	homotypic adhesion between pseudo-mesenchymal activated cells	$10^{-5} \ [\mu m/\mu g \, s]$
$F_{\mathrm{r}}^{\mathrm{M}^+\mathrm{M}}$	heterotypic intercellular repulsion	$10^{-4} \ [\mu m/\mu g \, s]$
$F_{\mathrm{a}}^{\mathrm{M}^+\mathrm{M}}$	heterotypic intercellular adhesion	$10^{-5} \ [\mu m/\mu g \, s]$
$F_{\mathrm{r}}^{\mathrm{EM}}$	heterotypic intercellular repulsion	$10^{-3} \ [\mu m/\mu g \, s]$
$F_{\mathrm{a}}^{\mathrm{EM}}$	heterotypic intercellular adhesion	$10^{-4} \ [\mu m/\mu g \, s]$
$F_{\mathrm{r}}^{\mathrm{EM}^+}$	heterotypic intercellular repulsion	$0.1 \ [\mu m/\mu g \, s]$
$F_{\mathrm{a}}^{\mathrm{EM}^+}$	heterotypic intercellular adhesion	$1 \ [\mu m/\mu g \, s]$
$F_{\mathrm{r}}^{\mathrm{EE}}$	homotypic repulsion between fully epithelial cells	$0.01 \ [\mu m/\mu g \, s]$
$F_{\mathrm{a}}^{\mathrm{EE}}$	homotypic adhesion between fully epithelial cells	$0.01 \ [\mu m/\mu g \, s]$

given by

$$
\begin{cases}
\mathbf{X}^{\mathrm{M}}(t) = \{\mathbf{x}_1^{\mathrm{M}}(t), \ \mathbf{x}_2^{\mathrm{M}}(t), \ \ldots, \ \mathbf{x}_{\mathrm{N_M}(t)}^{\mathrm{M}}\}, \\[2mm]
\mathbf{X}^{\mathrm{M}^+}(t) = \{\mathbf{x}_1^{\mathrm{M}^+}(t), \ \mathbf{x}_2^{\mathrm{M}^+}(t), \ \ldots, \ \mathbf{x}_{\mathrm{N_{M^+}}(t)}^{\mathrm{M}^+}\}, \\[2mm]
\rho^{\mathrm{E}}(t, \mathbf{y}) \ : \ \int_{\Omega} \rho^{\mathrm{E}}(t, \mathbf{y})d\mathbf{y} \ = M_{\mathrm{E}}(t) = \overline{m}\, N_{\mathrm{E}}(t) \ \ \forall \, \mathbf{y} \in \Omega.
\end{cases}
\tag{21}
$$

It is useful to notice that, while the number of cells belonging to each clone can vary due to possible differentiation, the total number of cells forming the primordium does not change (i.e., $\mathrm{N_M}(t) + \mathrm{N_{M^+}}(t) + \mathrm{N_E}(t) = N$). As it is out of the scope of this article, we do not describe the molecular fgf-induced cascades leading to the transition $\mathrm{M} \to \mathrm{M}^+$. In this respect, the location of such cell differentiations is established *a priori* (however accounting for proper spatial determinants). We further assume that, as soon as a pseudo-mesenchymal cell

passes to the activated clone, the surrounding individuals react acquiring the fully epithelial fate (i.e., M → E). In particular, such a phenotypic transition involves only the cells located at a distance from the activated mesenchymal individual lower than $2\,r_c$ (where r_c has been introduced in Eq. (5), but in this context it results equal to $5\,\mu$m, with the consequent reduction of the cell mass $\overline{m}$ to $0.2 \cdot 10^{-3}\,\mu$g). This models the fact that the epithelialization is induced by the M$^+$-type cells via contact signaling occurring through transmembrane proteins. In mathematical terms, assuming the activation of a pseudo-mesenchymal cell $\mathbf{x}_k^{\mathrm{M}}$, the processes leading to the formation of a single rosette can be described as:

$$
\begin{cases}
N^{\mathrm{M}}(t^+) = N^{\mathrm{M}}(t) - (1 + P(t)); \\[2mm]
N^{\mathrm{M}^+}(t^+) = N^{\mathrm{M}^+}(t) + 1; \\[2mm]
M^{\mathrm{E}}(t^+) = M^{\mathrm{E}}(t) + \overline{m}P(t); \\[2mm]
\mathbf{X}^{\mathrm{M}}(t^+) = \mathbf{X}^{\mathrm{M}}(t) \setminus \{\mathbf{x}_k^{\mathrm{M}}(t), \mathbf{p}_1^{\mathrm{M}}(t), \ldots, \mathbf{p}_{P(t)}^{\mathrm{M}}(t)\} = \{\mathbf{x}_i^{\mathrm{M}}(t)\}_{i=1}^{N^{\mathrm{M}}(t^+)}; \\[2mm]
\mathbf{X}^{\mathrm{M}^+}(t^+) = \mathbf{X}^{\mathrm{M}^+}(t) \cup \{\mathbf{x}_k^{\mathrm{M}}(t)\} = \{\mathbf{x}_j^{\mathrm{M}^+}(t)\}_{j=1}^{N^{\mathrm{M}^+}(t^+)}; \\[2mm]
\rho^{\mathrm{E}}(t^+, \mathbf{y}) = \rho^{\mathrm{E}}(t, \mathbf{y}) + \sum_{h=1}^{P(t)} w_{\mathbf{p}_h^{\mathrm{M}}}(\mathbf{y}) \quad \forall\, \mathbf{y} \in \Omega;
\end{cases}
\tag{22}
$$

where $\mathbf{p}_1^{\mathrm{M}}, \ldots, \mathbf{p}_P^{\mathrm{M}} \in \mathcal{B}_{2r_c}(\mathbf{x}_k^{\mathrm{M}}(t))$ are the positions of $P(t)$ mesenchymal cells that pass to the epithelial clone at a given time t.

As already described, in the first stage of development, the primordium has not a directional migration. Indeed, its component cells (regardless of their phenotype) are only subjected to homotypic and heterotypic adhesive interactions, that suffice to maintain the cohesion of the proto-organ while preserving single cell dimensions. In this respect, cell dynamics are regulated by the following hybrid PDE/ODE system:

$$
\begin{cases}
\dfrac{d\mathbf{x}_i^{\mathrm{M}}(t)}{dt} = \mathbf{v}_{\mathrm{M}}(\mathbf{x}_i^{\mathrm{M}}(t)), \quad i = 1, \ldots, \mathrm{N}^{\mathrm{M}}(t); \\[4mm]
\dfrac{d\mathbf{x}_j^{\mathrm{M}^+}(t)}{dt} = \mathbf{v}_{\mathrm{M}^+}(\mathbf{x}_j^{\mathrm{M}^+}(t)), \quad j = 1, \ldots, \mathrm{N}^{\mathrm{M}^+}(t); \\[4mm]
\dfrac{\partial \rho^{\mathrm{E}}(t, \mathbf{y})}{\partial t} + \nabla \cdot (\rho^{\mathrm{E}}(t, \mathbf{y})\, \mathbf{v}_{\mathrm{E}}(t, \mathbf{y})) = 0 \quad \forall\, \mathbf{y} \in \Omega,
\end{cases}
$$

where the relative velocities read as

$$
\begin{cases}
\mathbf{v}_{\mathrm{M}}(\mathbf{x}_i^{\mathrm{M}}(t)) = \overline{m}\Big[\sum_{k=1}^{N^{\mathrm{M}}(t)} \mathbf{K}^{\mathrm{M\,M}}(\mathbf{x}_k^{\mathrm{M}}(t) - \mathbf{x}_i^{\mathrm{M}}(t)) + \\
\qquad + \sum_{h=1}^{N^{\mathrm{M}^+}(t)} \mathbf{K}^{\mathrm{M\,M}^+}(\mathbf{x}_h^{\mathrm{M}^+}(t) - \mathbf{x}_i^{\mathrm{M}}(t)) \Big] + \int_{\Omega} \mathbf{K}^{\mathrm{M\,E}}(\boldsymbol{\xi} - \mathbf{x}_i^{\mathrm{M}}(t))\rho^{\mathrm{E}}(t,\boldsymbol{\xi})\,d\boldsymbol{\xi}; \\[2ex]
\mathbf{v}_{\mathrm{M}^+}(\mathbf{x}_j^{\mathrm{M}^+}(t)) = \overline{m}\Big[\sum_{k=1}^{N^{\mathrm{M}}(t)} \mathbf{K}^{\mathrm{M}^+ \mathrm{M}}(\mathbf{x}_k^{\mathrm{M}}(t) - \mathbf{x}_j^{\mathrm{M}^+}(t)) + \\
\qquad + \sum_{h=1}^{N^{\mathrm{M}^+}(t)} \mathbf{K}^{\mathrm{M}^+ \mathrm{M}^+}(\mathbf{x}_h^{\mathrm{M}^+}(t) - \mathbf{x}_j^{\mathrm{M}^+}(t)) \Big] + \int_{\Omega} \mathbf{K}^{\mathrm{M}^+ \mathrm{E}}(\boldsymbol{\xi} - \mathbf{x}_j^{\mathrm{M}^+}(t))\rho^{\mathrm{E}}(t,\boldsymbol{\xi})\,d\boldsymbol{\xi}; \\[2ex]
\mathbf{v}_{\mathrm{E}}(\mathbf{y}) = \overline{m}\Big[\sum_{k=1}^{N^{\mathrm{M}}(t)} \mathbf{K}^{\mathrm{E\,M}}(\mathbf{x}_k^{\mathrm{M}}(t) - \mathbf{y}) + \sum_{h=1}^{N^{\mathrm{M}^+}(t)} \mathbf{K}^{\mathrm{E\,M}^+}(\mathbf{x}_h^{\mathrm{M}^+}(t) - \mathbf{y}) \Big] + \\
\qquad\qquad\qquad\qquad\qquad + \int_{\Omega} \mathbf{K}^{\mathrm{E\,E}}(\boldsymbol{\xi} - \mathbf{y})\rho^{\mathrm{E}}(t,\boldsymbol{\xi})\,d\boldsymbol{\xi};
\end{cases}
\tag{23}
$$

where the interaction kernels are defined as in Eq. (18), thereby reproducing isotropic adhesive/repulsive intercellular interactions. In particular, given $d_{\mathrm{r}} = 10\ \mu$m and $d_{\mathrm{a}} = 15\ \mu$m, the interaction between mesenchymal cells should be in a sort of equilibrium to preserve their initial positions. On the other hand, the interactions involving the epithelial mass density should be able to drive rosette formation and maintenance. The specific parameter values are listed in Table 4.

As reproduced in Fig. 7, we start the resulting simulation with a primordium composed of 100 inactivated pseudo-mesenchymal cells (i..e, of type "M"), placed in a domain Ω of size 200 μm $\times$ 50 μm (with mesh grid size $= 1\ \mu$ m). The specific cell pattern has been derived by a proper experimental image, the top-left panel of the figure. At $t_1 = 19$ h, a pseudo-mesenchymal cell located in (60 μm, 26 μm) is set to activate, triggering the formation of first anteriorly positioned rosette, which involve a phenotypic transition of 7-8 surrounding individuals. Over the next few hours, other two additional rosettes forms to the posterior, as the result of successive mesenchymal cell activations occurring in (110 μm, 25 μm) at $t_2 = 23$ h and in (141 μm, 29 μm) at $t_3 = 24$ h. It is finally worth noting that the model parameter setting allows to avoid nonphysical evolutions of the system, such as cell overlapping, dramatic compression of the epithelial mass density, or, conversely, disaggregation of the primordium.
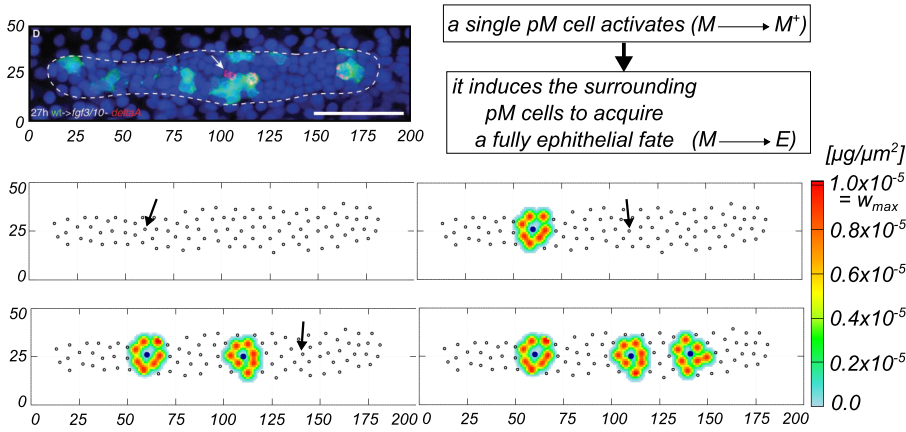
Fig. 7 First stage of the formation of the zebrafish posterior lateral line primordium. Top-left panel: Biological image of pLL primordium. Top-right panel: Sketch of the sequence of cell phenotypic transitions that lead to the formation of a rosette. Central-left panel: Initial condition of our numerical simulation. Central-right panel: First rosette forms in the pLL anterior. Bottom panels: Other two rosettes add at the posterior of the proto-organ. The black arrows indicate the pseudo-mesenchymal cells undergoing transition to the activated phenotype. For the readers' convenience, such differentiated individuals are represented by bigger dark dots.

4 Conclusions

A wide range of relevant biological systems is characterised by the coexistence of distinct clones of the same cell lineage, which have specific functions and migratory determinants. Furthermore, in such systems, cells are able to change their phenotype. For instance, in vasculogenesis, tumour growth and invasion, as well as in organogenesis and morphogenesis, relevant component processes result in fact from the specialization of few cells, that are able to activate and behave as a pattern guidance for the remaining part of the system. In this respect, we here propose a modelling framework where cells within an aggregate can be described either as a set of localized particles or as distributed masses, according to their biological behavior. Moreover, the modeling framework is enriched by a coherent procedure to reproduce cell phenotypic differentiation, i.e., to switch between the two mathematical representations via the use of a proper *bubble function*. A further feature of the proposed theoretical model is that it can include cell migratory dynamics and interactions, as well as growth mechanisms. The evolution of molecular substances, which possibly influence both cell motility and phenotypic differentiation, are taken also in account.

The proposed modeling approach is then here applied to selected biological problems, i.e., the avascular growth and invasion of a tumor mass and the first stages of pLL development. In the first case, a malignant spheroid is assumed to be composed of two cell phenotypes: a set of aggressive activated cells (represented by a pointwise mathematical description) and a quiescent mass (represented by a distributed density). In this respect, by changing the

values of relevant parameters, we can reproduce either the extension of tumor tongues or the spreading of metastasis. The description of the first stage of the pLL development requires instead the extension of the model to the case of three coexisting clones of the same cell lineage. Interestingly, the formation of rosettes can be represented by reproducing an inverse phenotypic differentiation, i.e., by employing a localized-to-distributed transition.

Future work developments will involve an in-depth analysis of the model stability with respect both to the parameter settings and to the specific choice of the form of the bubble function. Finally, in order to further assess the advantages of the proposed modelling framework, it will be interesting to apply the model to other biological problems whose evolution is characterized by cell phenotypic differentiations that preserve cell biophysical properties but lead to different behaviors.

References

1. Alberts B., Johnson A., Lewis J., Raff M., Roberts K., Walter P., Molecular Biology of theCell, 3rd Ed. Garland Science, New York, USA (2002)
2. Anderson A. R. A., Weaver A. M., Cummings P. T., Quaranta V., Tumor morphology and phenotypic evolution driven by selective pressure from the microenvironment, Cell, 127, 905 − 915 (2006)
3. Armstrong N. J., Kevin J. P., Sherratt J. A., A continuum approach to modelling cell-cell adhesion, J. Theor. Biol., 243, 98 - 113 (2006)
4. Armstrong N. J., Kevin J. P., Sherratt J. A., Adding adhesion to a chemical signaling model for somite formation, Bull. Math. Biol., 71, 1 - 24 (2009)
5. Bell H. S., Whittle I. R., Walker M., Leaver H. A., Wharton S. B., The development of necrosis and apoptosis in glioma: experimental findings using spheroid culture systems, Neuropathol. Appl. Neurobiol, 27, 291 − 304 (2001)
6. Brazma A., Parkinson H., Schlitt T., Shojatalab M., A quick introduction to elements of biology-cells, molecules, genes, functional genomics, microarrays, European Bioinformatics Institute, Draft, (2001)
7. Brown, J. M., Tumor microenvironment and the response to anticancer therapy. Cancer Biol. Ther. 1, 453 - 458 (2002)
8. Burleson K. M., Boente M. P., Parmabuccian S. E., Skubitz A. P., Disaggregation and invasion of ovarian carcinoma ascites spheroids, J. Transl. Med., 4, 1 − 16 (2006)
9. Castro M. A. A., Klamt F., Grieneisen V. A., Grivicich I., Moreira J. C. F., Gompertzian growth pattern correlated with phenotypic organization of colon carcinoma, malignant glioma and non-small cell lung carcinoma cell lines, Cell. Prolif., 36, 65 − 73 (2003)
10. Cavallaro U., Christofori G., Cell adhesion in tumor invasion and metastasis: loss of the glue is not enough, Biochim. Biophys. Acta, 1552, 39 − 45 (2001)
11. Christofori G., Changing neighbours, changing behaviour: cell adhesion molecule-mediated signalling during tumour progression, Embo. J., 22, 2318 − 2323 (2003)
12. Colombi A., Scianna M., Tosin A., Differentiated cell behaviour: a multiscale approach using measure theory, J. Math. Biol., 71, 5, 1049 − 1079 (2014)
13. Colombi A., Scianna M., Preziosi L., A measure-theoretic model for cell migration and aggregation, Math. Model. Nat. Phenom., 1, 32 − 63 (2015)
14. De Luca A., Arena N., Sena L. M., Medico E., Met overexpression confers HGF-dependent invasive phenotype to human thyroid carcinoma cells in vitro, J. Cell. Physiol., 180, 3, 365 − 371 (1999)

15. Di Costanzo E., Natalini R., Preziosi L., A hybrid mathematical model for self-organizing cell migration in the zebrafish lateral line, J. Math. Biol., 71, 171 – 214 (2015)

16. Friedl P., Gilmour D., Collective cell migration in morphogenesis, regeneration and cancer, Nat. Rev. Mol. Cell. Biol., 10, 445 – 457 (2009)

17. Gatenby R. A., Smallbone K., Maini P. K., Rose F., Averill J., Nagle R. B., Worrall L., Gillies R. J., Cellular adaptations to hypoxia and acidosis during somatic evolution of breast cancer, Br. J. Cancer., 97, 646 – 653 (2007)

18. Ghysen A., Dambly-Chaudire C., Development of the zebrafish lateral line, Curr. Opin. Neurobiol., 14, 67 – 73 (2004)

19. Hegedus B., Marga F., Jakab K., Sharpe-Timms K. L., Forgacs G., The interplay of cell-cell and cell-matrix interactions in the invasive properties of brain tumors, Biophys. J., 91, 2708 – 2716 (2006)

20. Hillen T., Painter K. J., Winkler M., Convergence of a cancer invasion model to a logistic chemotaxis model, Math. Models and Methods in Applied Sci, M3AS, 23, 1, 165 – 198 (2013)

21. Ilina O., Friedl P., Mechanisms of collective cell migration at a glance, J. Cell. Sci., 122, 3203 – 3208 (2009)

22. Khaitan D., Chandna S., Arya M. B., Dwarakanath B. S, Establishment and characterization of multicellular spheroids from a human glioma cell line: implications for tumor therapy, J. Transl. Med., 4, 12 – 25 (2006)

23. Khalil A. A., Friedl P., Determinants of leader cells in collective cell migration, Integr. Biol. (Camb), 2, 568 – 574 (2010)

24. Liu Z. J., Shirakawa T., Li Y., Soma A., Oka M., Dotto G. P., Fairman R. M., Velazquez O. C., Herlyn M., Regulation of Notch1 and Dll4 by vascular endothelial growth factor in arterial endothelial cells: implications for modulating arteriogenesis and angiogenesis, Mol. Cell. Biol., 23, 14 – 25 (2003)

25. Nechipokur A., Raible D. W., FGF-dependent mechanosensory organ patterining in zebrafish, Science, 320, 1774 (2008)

26. Painter K. J., Bloomfield J. M., Sherratt J. A., Gerlsch A., A nonlocal model for contact attraction and repulsion in heterogeneous cell populations, Bull. Math. Biol. (2015)

27. Puiffe M. L., La Page C., Filali–Mouhim A., Zietarska M., Ouellet V., Toniny P. N., Chevrette M., Provencher D. M., Mes–Masson A. M., Characterization of ovarian cancer ascites on cell invasion, proliferation, spheroid formation, and gene expression in an in vitro model of epithelial ovarian cancer, Neoplasia, 9, 820 – 829 (2007)

28. Scianna M., Bassino E., Munaron L., A cellular Potts model analyzing differentiated cell behavior during in vivo vascularization of a hypoxic tissue, Computers in Biology and Medicine, 63, 143 – 156 (2015)

29. Scianna M., Bell C. G., Preziosi L., A review of mathematical models for the formation of vascular networks, J. Theor. Biol., 333, 174 – 209 (2013)

30. Scianna M., Preziosi L., Multiscale developments of cellular Potts models, Mult. Model. Sim., 10, 342 – 382 (2012)

31. Shield K., Ackland M. L., Ahnmed N., Rice G. E, Multicellular spheroids in ovarian cancer metastases: biology and pathology, Gynec. Oncol. 113, 143 – 148 (2008)

32. Smolle J., Fractal tumor stromal border in a non-equilibrium growth model, Anal. Quant. Cytol. Histol., 20, 7 – 13 (1998)

33. Stein A. M., Demuth T., Mobley D., Berens M., Sander L. M., A mathematical model of glioblastoma tumor spheroid invasion in a three-dimensional in vitro experiment, Biophys. J. 92, 356 – 365 (2007)

34. Sundfeldt K., Cell-cell adhesion in the normal ovary and ovarian tumors of epithelial origin; an exception to the rule, Molecular and Cellular Endocrinology 202, 89 – 96 (2003)

35. Turner S., Sherratt J. A., Intercellular adhesion and cancer invasion: a discrete simulation using the extended Potts model, J. Theor. Biol., 216, 85 – 100 (2002)

36. Weidner K. M., Behrens J., Vandekerckhove J., Birchmeier W., Scatter factor: molecular characteristics and effect on the invasiveness of epithelial cells, J Cell Biol, 111, 2097–2108 (1990)

37. Williams C. K., Li J. L., Murga M., Harris A. L., Tosato G., Upregulation of the Notch ligand delta-like 4 inhibits VEGF induced endothelial cell function, Blood, 107, 931 – 939 (2006)
38. Wise S. M., Lowengrub J. S. , Frieboes H. B., Cristini V., Threedimensional multispecies nonlinear tumor growth: model and numerical method, Int. J. Oncol., 253, 524 – 543 (2008)